Investigation of instantaneous and local transmembrane pressure in rotating and vibrating filtration (RVF) module: Comparison of three impellers

Ming Cheng, Claude Le Men, Alain Line, Philippe Schmitz, Luc Fillaudeau

▶ To cite this version:

Ming Cheng, Claude Le Men, Alain Line, Philippe Schmitz, Luc Fillaudeau. Investigation of instantaneous and local transmembrane pressure in rotating and vibrating filtration (RVF) module: Comparison of three impellers. Separation and Purification Technology, 2022, 280, 10.1016/j.seppur.2021.119827 . hal-03450507

HAL Id: hal-03450507

https://hal.inrae.fr/hal-03450507

Submitted on 16 Oct 2023

HAL is a multi-disciplinary open access archive for the deposit and dissemination of scientific research documents, whether they are published or not. The documents may come from teaching and research institutions in France or abroad, or from public or private research centers.

L'archive ouverte pluridisciplinaire **HAL**, est destinée au dépôt et à la diffusion de documents scientifiques de niveau recherche, publiés ou non, émanant des établissements d'enseignement et de recherche français ou étrangers, des laboratoires publics ou privés.

Distributed under a Creative Commons Attribution - NonCommercial 4.0 International License

Version of Record: https://www.sciencedirect.com/science/article/pii/S1383586621015343
Manuscript_d0ad269745084c515aef5cc84ccae217

Investigation of instantaneous and local transmembrane pressure in Rotating and Vibrating Filtration (RVF) module: comparison of three impellers

Ming Cheng[1*], Claude Le Men[1,2], Alain Line[1,2], Philippe Schmitz[1,2], Luc Fillaudeau[1,2]

[1]TBI, Université de Toulouse, CNRS UMR5504, INRA UMR792, INSA, 31055, 135, avenue de Rangueil, Toulouse, France

[2]Federation de Recherche FERMAT (FR 3089), Université de Toulouse, CNRS, INPT, INSA, UPS, Toulouse, France

Abstract: The instantaneous and local pressure at membrane surface was experimentally investigated in a dynamic filtration module, named Rotating and Vibrating Filtration (RVF) module. The present paper focuses mainly on the pressure fluctuations in turbulent regime. To this end, the instantaneous pressure is decomposed into its time-averaged and fluctuating quantities using Statistical Analysis (SA), Probability Distribution Function (PDF) and Fast Fourier Transform (FFT). The effects of back pressure, flowrate, rotation frequency and radial position at the membrane on the magnitude of the pressure fluctuations are studied for three different impellers (Imp 1, 2 and 3). For mixing pressure, Imp 2 (6 blades) exhibits a larger core velocity coefficient than Imp 1 and Imp 3 (3 blades). For pressure fluctuation, the extracted variables from SA (standard deviations), PDF (peak-to-peak values) and FFT (amplitudes) confirm that the magnitude of Imp 1> Imp 3> Imp 2. Considering SA at 20 Hz, standard deviation of Imp 1 exceeds 100 mbar (up to 25% of TMP), while these values are negligible (<10%) for Imp 2 and 3. After FFT, the dominant frequency identified with Imp 1 is equal to 3 times the rotation frequency (*3N*). Conversely, different frequencies (*6N*, *3N* and *N*) exhibiting low amplitude are observed for Imp 2 and 3. Based on the PDF modelling, periodic and random contributions are extracted by deconvolution. Then, the empirical correlations are established to estimate their intensities as a function of rotation frequency and radial position. A "resonance frequency" of 21.1 Hz is clearly identified with Imp 1.

Keywords: Instantaneous pressure; impeller configurations; core velocity coefficient; pressure fluctuation; resonance frequency; signal reconstruction.

Highlights:

1. Comparison of local pressure at membrane surface for three impellers;
2. Determination of local core velocity coefficient;
3. Decomposition of signal with periodic and random contributions;
4. Analysis of peak amplitudes and dominant frequencies;
5. Signal reconstruction with established empirical correlations.

© 2021 published by Elsevier. This manuscript is made available under the CC BY NC user license
https://creativecommons.org/licenses/by-nc/4.0/

Table of content

1 Introduction

Dynamic filtration (DF) is defined as the mechanical movement of devices or membranes to generate a high stress (shear rate and pressure) at the membrane surface. The external forces induced by rotation, oscillation and/or vibration show great promise for controlling fouling, cake formation and mitigating concentration polarization. This results in uncoupling between local shear rate and transmembrane pressure (TMP) from feeding flowrate [1]. In consequence, DF is considered to be energy-saving (power/flux) compared to the conventional dead-end and cross-flow filtration [2, 3]. However, due to the complex geometries and configurations of DF, the study of its internal hydrodynamics remains a great challenge.

Based on the hydrodynamic approaches, the technologies to create instabilities of flow may contribute to reducing concentration polarization and fouling at the membrane surface [4], and shear-based studies have been reported extensively [1, 5-8]. In rotating system, the shear rate has been enhanced by changing the shape of the rotor [9-11], or by adding the insert [12] in the filtration cell. Some studies have achieved a higher shear rate via overlapping membrane discs on one or more shafts [13]. For cylindrical filters, the Taylor vortices generated between the annular gap greatly increase the mixing effect in laminar flow; increasing the rotation speed, Taylor vortices degenerate into turbulent flow [2, 14]. In oscillating system, flat disk, rectangular, cylinder or hollow fibre membranes were mounted on the fixed shaft for transverse, longitudinal or azimuthal vibration [15-19]. Wu et al. [20] reported the installation of a vibrating spacer close to the submerged flat sheet membranes for fouling control. It suggested that the turbulence promoter contributes to the enhancement of turbulent kinetic energy and membrane surface shear rate.

The hydrodynamics in the DF modules have been carried out in order to evaluate and estimate the filtration performances. Global approaches associated with dimensionless correlations, such as Reynolds number versus Darcy’s and power number were established to model the power consumption [1, 21]. Semi-local approaches include the additional pressure and local shear rate. In rotating systems, the mixing pressure caused by the rotating disk or impeller is related to the core velocity coefficient, but this theory has not been reported in vibrating systems. The empirical correlations to estimate local shear rate were promoted according to the operating conditions and specific cell geomatics [1]. For local approaches, the experimental measurement allows the visualization of velocity, pressure and shear fields, followed by the comparison to computational fluid dynamics (CFD) technology [22-24].

Some researchers have found the empirical relations between steady-state permeate flux and local shear rate [5, 25, 26]. The average shear rate is commonly used as a primary indicator for evaluating filtration systems. In spite of the fact that an increase in shear implies a higher permeate flux, it is also essential to account for the unit energy consumption, irreversible fouling and fluid sensitivity. The theory of critical and threshold flux was promoted in order to limit the increase of foulant, with the relevant TMP usually being a time-mean value [27, 28]. In rotating disk module, the disk with vans yields higher permeate flux than smooth discs at the same shear rate [29], the explanation of which may be attributed to the stress (shear and pressure) fluctuation. In microfiltration, transmembrane pressure can be maintained at very low values (~100 mbar), and then high-pressure fluctuation (same order of magnitude than TMP) could contribute to surface cake layer and internal reversible fouling destabilization.

In a previous study [30], the instantaneous and local pressures at the membrane surface were investigated during the rotation with a three-blade impeller. The time series pressures were treated to extract the fluctuating information (intensity and frequency), which showed to be affected by the radius and rotation frequency. In the present study, the effects of back pressure, flowrate and impeller configurations (number and shape of blades) on pressure fluctuations were investigated on time and frequency domain. According to the Probability Distribution Function (PDF), the fluctuating signals were decomposed into the representative of periodic and random components. Thus, the dominant frequencies, intensities of periodical and random contributions constitute the pressure fluctuation; the core velocity coefficient allows to estimate of the mixing pressure. Finally, the reconstructed instantaneous pressures were achieved by the sum of steady pressure and fluctuating components and then compared with the experimental data.

2 Materials and methods

2.1 Experimental set-up and instrumentation

2.1.1 RVF module

The lab-scale RVF module [22, 31] consists of two filtration cells (0.2 L per cell, 1.5 L in total), both of which equips with an impeller rotate with the central shaft. The rotation frequency N refers to the central shaft (impeller), with a maximum value of 50 Hz. Fig. 1a shows the schematic diagram of one filtration cell. Two crown membranes ($R_0=25$ mm, $R_m=67$ mm) can be mounted on the porous substrates that allow the collection of permeate to the lateral ducts. In order to achieve an accurate measurement of the instantaneous pressure on the membrane surface, the 8 pressure taps with 2 mm diameter are distributed over a radius ranging from R1 to R8. Three impellers with two shapes of blades (shape 1 has increased surface area and 8 mm thickness; shape 2 has decreased surface area and thickness) are applied in the tests, as shown in Fig. 1b and c. Imp 1 equips with three blades (shape 1); Imp 2 and 3 have six and three blades (shape 2), respectively.

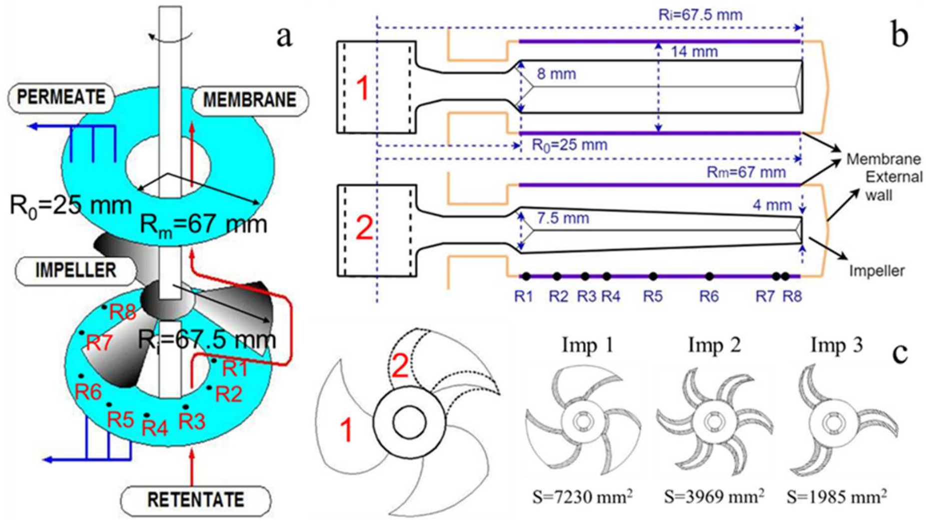

Fig. 1 Schematic diagram of Rotating and Vibrating Filtration module. (a) one filtration cell; (b) rotating impellers in the filtration cell; (c) three types of the impeller.

2.1.2 Experimental set-up

In Fig. 2, the experimental set-up constitutes the feeding tank, circulation loop and RVF module. During the experiments, the fluid is pumped from a double-jacket tank (8 L) into the RVF module. The permeate is closed, and retentate is fed back to the tank. The feeding flowrate is controlled by a volumetric pump (Pump) and acquired with a mass flowmeter (MF) in the outlet. It enables the measurement of flowrate (Q_F), density (ρ) and outlet temperature (T_{outlet}). The inlet temperature is recorded from the conductivity sensor Cond (T_{inlet}) in the feeding tank, to be maintained at 20±5 °C with thermal regulation. The back pressure is measured by a relative pressure sensor (PR1, Bourdon-Haenni Y913, 0/6 bar, ±0.2% full scale) and adjusted by a counter-pressure valve coupled with a pressure gauge (PG, 0/4 bar). Another relative pressure sensor (PR2, Killer, -1/+1 bar, ±0.2% full scale, maximum acquisition frequency 5 kHz) locates at the distributed stainless tubes of a home-designed porous substrate, which permits the instantaneous pressure measurements without membrane.

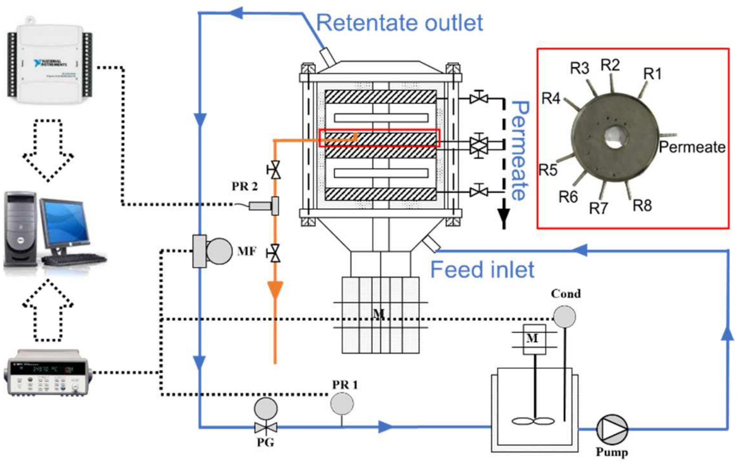

Fig. 2 Experimental set-up and data acquisition systems (dash line: permeate outlet, closed during the measurement; dotted lines: data acquisition channels. red frame: home-designed porous substrate;

orange line: instantaneous pressure measurement).

2.1.3 Operating conditions and data acquisition

In cross-flow microfiltration, the ratio between the average feed rate and permeability under turbulent conditions is higher than 10,000 [32]. This phenomenon also occurs in the applications of RVF module in wine making and brewing [31, 33]. Therefore, the suction effect can be neglected. Then, the experiments were carried out without permeate (no membrane was used) and back pressure at 300 mbar to avoid cavitation caused by the high rotation frequency. Tap water was used as feed fluid with flowrates up to 300 L/h. The instantaneous and local pressure at 8 radii from R1 to R8 (26.2-64.9 mm), different rotation frequencies (0-50 Hz) and rotating impellers were achieved.

In the tests, the operating conditions include the feeding flowrates, back pressure and temperature along the circulation loop were recorded by Agilent 34972A (Agilent Technologies, Loveland, USA) with the 3 s time interval. In contrast to these global measurements, local pressure was measured with PR2 and access to the NI USB-6009 (National Instruments, USA, 1 kHz) with a sampling frequency of 1000 Hz for more than 40 s.

2.2 **Data treatment**

Instantaneous pressure at the membrane surface can be classically decomposed into the sum of the steady pressure $\bar{P}(r)$ and the pressure fluctuations $\tilde{P}(r,t)$, as shown in Eq. (1). The evolution of the pressure field depends on the operating conditions. By considering another variable rotation frequency (*N*) in the experiments, the steady pressure and pressure fluctuation are given as $\bar{P}(N,r)$ and $\tilde{P}(N,r,t)$ in the following analysis, respectively.

$$P(r,t) = \bar{P}(r) + \tilde{P}(r,t) \tag{1}$$

2.2.1 Time domain analysis

The mean local pressure or steady pressure $\bar{P}(N,r)$ at the membrane surface is given in Eq. (2). Based on Navier Stokes equation, in cylindrical coordinates, and considering inviscid fluid and angular velocity is the main component, mean local pressure can be represented by Bernoulli's equation (Eq. (3)) [9]. Its value is equal to the sum of P_0 and ΔP_{mixing}. P_0 is the local pressure of the steady flow without rotation. ΔP_{mixing} is the mixing pressure given by the rotation of the impeller, the value of which is determined by the mean velocity $\bar{u}$ in the main fluid. In turbulent regime, the angular velocity $2\pi Nr$ generated by the rotating disk is much higher than radial and vertical velocity. The mean velocity in the flow can be represented as $\bar{u}$ equal to $k \cdot 2\pi Nr$, where k is the core velocity coefficient and inferior to 1 [30, 31, 33], ρ is the density. With the mean steady pressure, the experimental k value can be determined.

$$\bar{P}(N,r) = \frac{1}{m}\sum_{i=1}^{m} P(N,r,t_i) \tag{2}$$

$$\bar{P}(N,r) = P_0 + \Delta P_{mixing} = P_0 + \frac{1}{2}\rho\bar{u}^2 = P_0 + \frac{1}{2}\rho(k \cdot 2\pi Nr)^2 \tag{3}$$

The standard deviation of instantaneous pressure σ_P has been used to describe the intensity of the fluctuations [30], where m represents the sampling number. The coefficient, β is defined as the ratio between σ_P and $\bar{P}(N,r)$, and give the relative standard deviation.

$$\sigma_P{}^2 = \frac{1}{m}\sum_{i=1}^{m}(P(N,r,t_i) - \bar{P}(N,r))^2 \tag{4}$$

$$\beta = \frac{\sigma_P}{\bar{P}(N,r)} \times 100\% \tag{5}$$

Higher-order moments are useful to better characterize the Probability Distribution Function of the signal. Among them, skewness (S) is known as the normalized central moment of the third order, associate with the symmetry of the signal in PDF.

$$S = \frac{1}{m\sigma_P^3}\sum_{i=1}^{m}(P(N,r,t_i) - \bar{P}(N,r))^3 \tag{6}$$

Flatness (F) is the normalised central moment of the fourth order. It indicates the sharpness of the distribution.

$$F = \frac{1}{m\sigma_P^4}\sum_{i=1}^{m}(P(N,r,t_i) - \bar{P}(N,r))^4 \tag{7}$$

2.2.2 Frequency domain analysis

For frequency domain analysis, the dominant frequencies and their respective amplitudes are found using the Fast Fourier Transform (FFT). As shown in Eq. (8), the discrete function of Fourier Transform is displayed as a complex, where f is the frequency and m is the number of sampling points. The amplitude at the given frequency A_f is calculated as Eq. (9).

$$P(f) = \sum_{i=0}^{m-1} \tilde{P}(N,r,t_i)e^{-\frac{2\pi jfi}{m}}, \qquad f = 0,1,\ldots,m-1 \tag{8}$$

$$A_f = \frac{2}{m}\sqrt{P(f)^2} \tag{9}$$

2.2.3 Modelling

Based on the PDF, the pressure fluctuations are decomposed into periodic and random contributions. Both terms have been identified in the methodology paper previously [30]. The periodic component is simplified as a single sinusoidal wave, whereas the random component follows the normal distribution, shown as:

$$\widetilde{P_P}(t) = Asin(2\pi ft + \varphi) \tag{10}$$

$$\widetilde{P_R}(t) \sim Norm(\bar{x}, \sigma^2) \tag{11}$$

where A is the amplitude, f is the frequency, φ is the phase; $\bar{x}$ is the mean value of random signal equal to 0, σ means the standard deviation.

From the simulated functions, the model PDF is built by the convolution of PDF for both terms, as described below:

$$PDF_{model} = \frac{1}{\pi\sqrt{A^2 - x^2}} * \frac{1}{\sigma\sqrt{2\pi}} e^{-\frac{1}{2}(\frac{x-\bar{x}}{\sigma})^2} \tag{12}$$

By comparing the experimental data and model in PDF, two constants A and σ are obtained by minimising the cumulative error function Δ. *It* is defined as:

$$\Delta = Min\left(\sum_{i=0}^{100}\sqrt{\left(PDF_{exp} - PDF_{model}\right)^2}\right) \tag{13}$$

The fluctuating intensities of periodic (I_P) and random (I_R) components can be represented as $A/\sqrt{2}$ and σ, respectively. Thus, the sum of both contributions indicates the total energy input, or as the total fluctuation intensity.

3 Results and discussion

As demonstrated previously, the evolution of moment of the first order, the centre moment of second order, the nominalized centre moments of third and fourth order tend to converge with respect to the number of sampling points m superior to 1000 [30]. The following analyses include Statistical Analysis (SA), PDF and FFT, based on the raw data length equal to 2^{15} points. In order to establish the empirical model to estimate the local pressure, the raw signal is decomposed into continuous and fluctuating components.

3.1 **Raw data**

Instantaneous pressures were locally measured at eight radii (R1 to R8) and different rotation frequencies from 0 to 50 Hz. They are shown in Fig. 3, indicating the increase of steady pressure versus N and r. Interestingly, Imp 1 and 2 have similar steady pressure values, both higher than Imp 3. In addition, the magnitudes of pressure fluctuations for Imp 1 are more remarkable compared to Imp 2 and 3. In Fig. 3d, it can be observed that the instantaneous pressure for Imp 1 varies with a period around 60 Hz, which is consistent with three times the rotation frequency. This can be attributed to the number of blades. Whereas in Fig. 3f, the periodic amplitude of Imp 3 at 20 Hz is relatively small, its period is also in accordance with *3N*. For Imp 2 at 20 Hz, the periodic variation cannot be achieved from Fig. 3e, and the pressure fluctuations are much weaker. Further analysis is associated with the continuous component of the signal (steady pressure) and the pressure fluctuations defined in Eq.

(1).

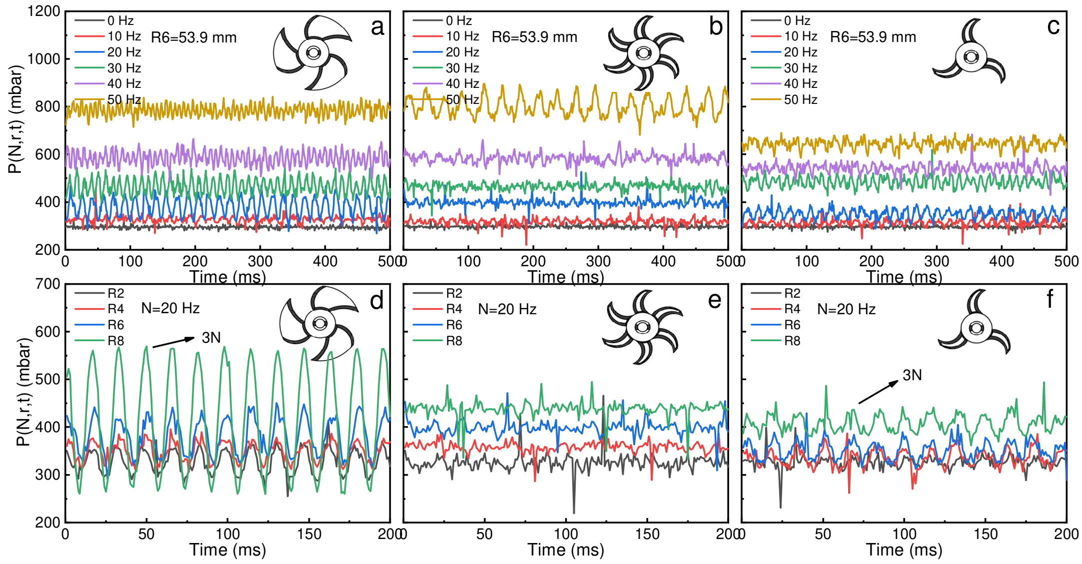

Fig. 3 Raw data analysis. (a), (b) and (c) are the evolution of instantaneous pressure versus rotation frequency for three impellers at R6; (d), (e) and (f) are the evolution of instantaneous pressure versus local radius for three impellers at 20 Hz.

3.2 Continuous components

The continuous pressures compose of P_0 and ΔP_{mixing}. The former is dependent on the back pressure and feeding flowrate, while the latter varies with rotation frequency and radius.

3.2.1 Mixing pressure

The mixing pressures as a function of rotation frequency and radius are presented in Fig. 4. In the global overview, it can be seen that Imp 1 and 2 generate the same level of additional pressure, and superior to Imp 3.

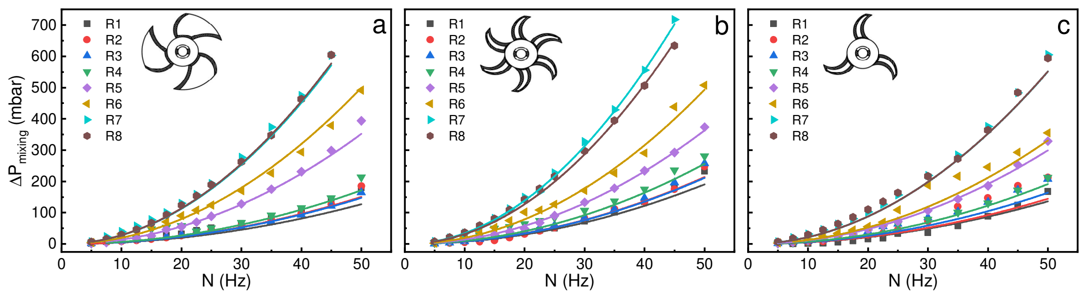

Fig. 4 Mixing pressures as a function of rotation frequency and radius. (a) Imp 1; (b) Imp 2; (c) Imp 3.

3.2.2 Core velocity coefficient

In rotating systems, the angular velocity in the main fluid can be written as $k \cdot 2\pi N$. As the tangential velocity is considered as the dominant component of the velocity vector, the additional pressure due to mixing can be approximated as proportional to N^2r^2, i.e., the square of the tangential velocity component. Therefore, it appears that the value of k larger than the actual value [30]. Fig. 5 shows the calculated k values as a function of the radius for the three different impellers. An increase of k can be observed at a lower radius, it might be explained by the highest contribution of radial velocity at the entrance of the cell (close to the shaft). Another decrease is found at the highest radius, which can be attributed to the reduction of local velocity close to the external wall [34]. By the regression of mixing pressure at all the conditions (rotation frequencies and radii), the core velocity coefficient follows the order: Imp 2>Imp 1>Imp 3 (0.63>0.59>0.54). It can be concluded that more blades and a larger surface area seem to increase k value. Similar results can be found in the rotating disk with vans [6, 29].

As reported in the literature, k value for the rotating flat disk is inferior to 0.45, above which occurs with rotating impeller or disk with vans [1]. In comparison to the full disk, the additional force generated by the rotating impeller includes the push force at the leading edge and the differential pressure force between the leading and trailing edge of the blade, apart from the shear force on the plate [29, 30]. Therefore, the complex geometry of the impeller may be hard to estimate the local shear stress at the membrane surface.

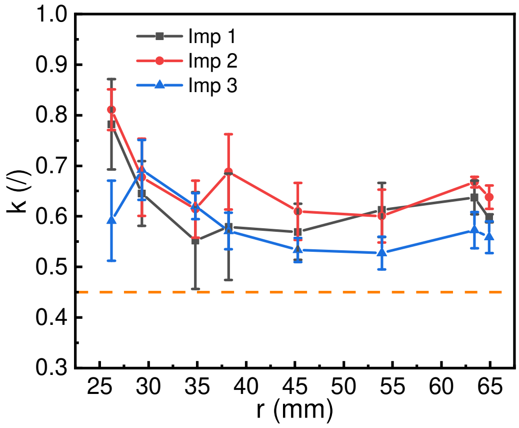

Fig. 5 Core velocity coefficient at the various radius. The dashed line indicates the k value at the boundary between the rotating flat disk ($0.31<k<0.45$) and the rotating disk with vans or impeller ($0.45\leq k<0.9$).

3.3 Fluctuating components

Previously, the pressure fluctuations have been analysed with SA, PDF, FFT and modelled [30]. Similar treatments are carried out to compare the fluctuations in terms of amplitudes and frequencies with three different impellers.

3.3.1 SA

3.3.1.1 Standard deviation

The standard deviation σ_P has been used to describe the fluctuation intensity of the signal. As shown in Fig. 6, pressure fluctuations are independent of back pressure and flowrate, but influenced by rotation frequency. On the contrary, the local pressure

P_0 is influenced by these parameters.

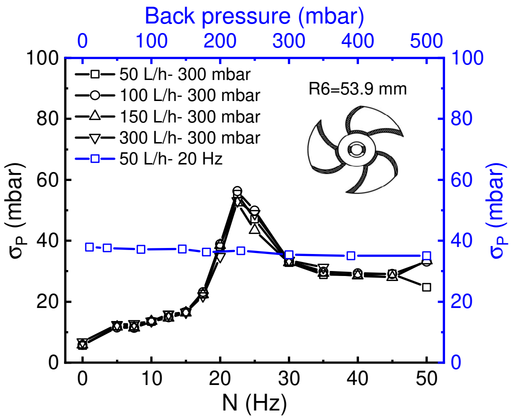

Fig. 6 Standard deviation of instantaneous pressure for Imp 1 at different conditions (flowrates, rotation frequencies and back pressures).

Fig. 7a, b and c present the evolution of the standard deviation at different conditions. For Imp 1, a large increase of σ_P with N can be observed below 20 Hz, and followed by a decrease until 50 Hz. The maximum σ_P fluctuates in the range of rotation frequency between 20 and 25 Hz. It increases with local radius, even reaches more than 100 mbar at R8. For Imp 2, σ_P exhibits a constant value below 20 mbar, and then slightly increases with a rotation frequency from 40 to 50 Hz. While the increase of σ_P occurs at 20 Hz with Imp 3, it is relatively lower than Imp 1. With the same shape of blades, the highest deviations for Imp 2 and 3 are limited to a value below 50 mbar, almost negligible when compared with Imp 1. It can be concluded that more blades contribute positively to a higher mixing pressure but negatively to the generation of pressure fluctuations. Comparing the standard deviation of instantaneous pressure relative to steady pressure, the coefficients of variation β are shown in Fig. 7d, e and f. It can be noticed that the β value of Imp 2 is limited to less than 7%; Imp 3 shows an increase, reaching 13% at R4. However, these values are inferior to Imp 1, which achieved 25.3% of local pressure at R8. It indicates that the pressure fluctuations cannot be neglected with Imp 1. An intensive fluctuating area with high-pressure fluctuations at the membrane surface is promoted as the range of rotation frequency from 15 to 30 Hz.

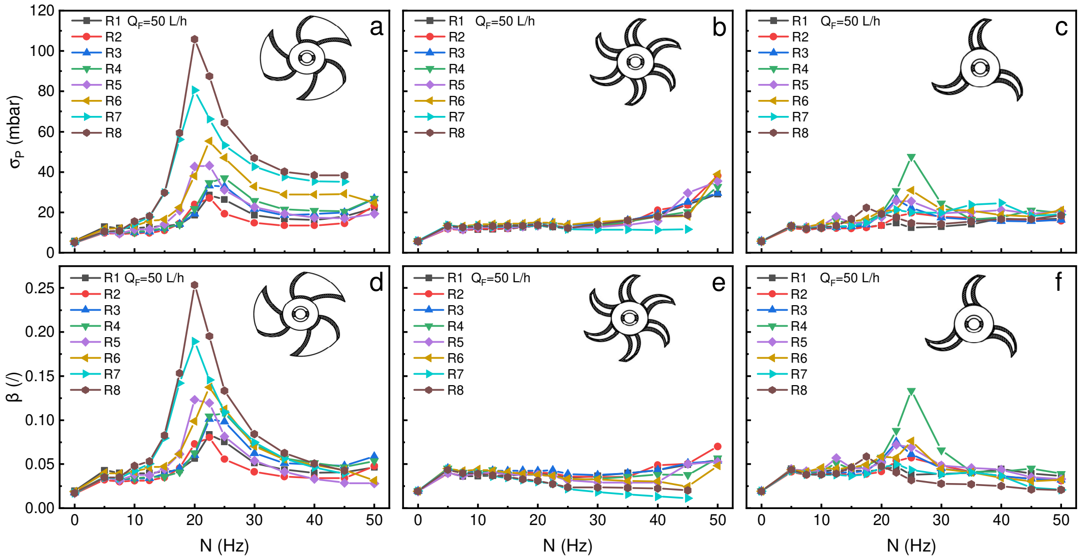

Fig. 7 Statistical Analysis. (a), (b) and (c) are the evolution of standard deviation versus rotation frequency for three impellers; (d), (e) and (f) are the coefficient of variation versus rotation frequency for three impellers.

3.3.1.2 Skewness and Flatness

The high order moment distributions from 0 to 50 Hz and R1 to R8 are shown in Fig. 9. Fig. 9a, b and c present the skewness under different conditions, with values fluctuating from -0.8 to 0.8 and show disorder for rotation frequency and local radius. The flatness indicates the degree of peakedness of PDF, as shown in Fig. 9 d, e and f. Compared with F in a normal distribution ($F=3$, dashed blue lines), the value of F superior to 3 informs that a sharp distribution with a narrow fluctuation intensity, while $F<3$ indicates the extension of PDF and results in a large deviation. For Imp 2, F shows a decrease with the rotation frequency, and its value is consistent with a normal distribution when the maximum speed of 50 Hz is reached. That can be explained by the increase in pressure fluctuations. The same results are also achieved from Imp 1 and 3. Comparison with the normal distribution gives an indication of the fluctuations in the data to some extent, but the magnitude of the fluctuations still needs further analysis.

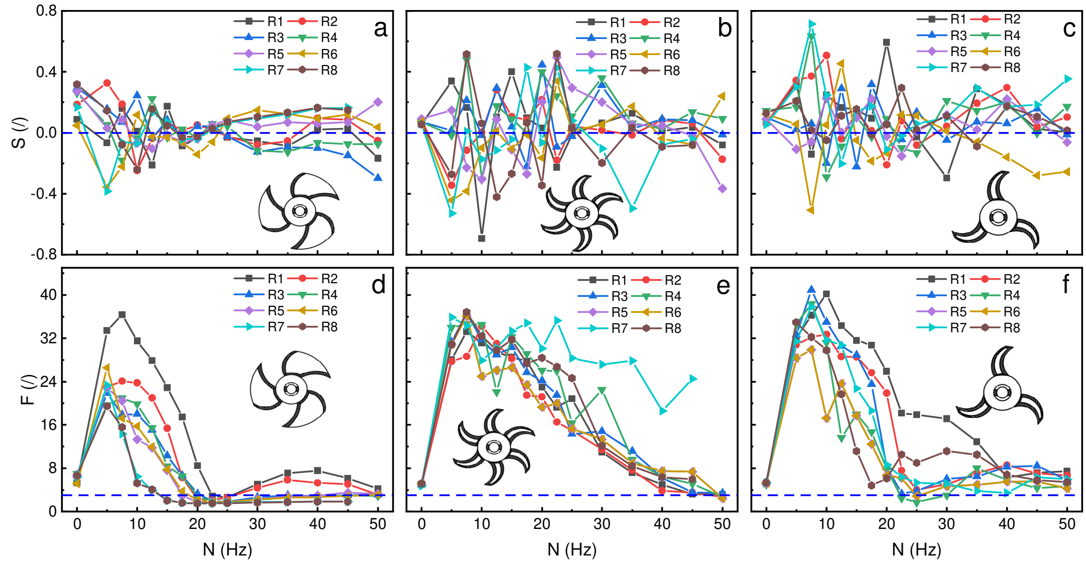

Fig. 8 High order items distribution. (a), (b) and (c) are the skewness distribution for three impellers; (d), (e) and (f) are the flatness distribution for three impellers. The dashed line indicates the S and F for normal distribution.

3.3.2 PDF

PDF provides a more explicit profile of pressure fluctuations. Fig. 9 presents the PDF of three impellers at different conditions. At R6, a strong fluctuation occurs at a rotation frequency around 20 Hz for Imp 1. The same observation can be found for Imp 3, but with lower fluctuation intensity. While the large extension of PDF for Imp 2 only finds at 50 Hz. At the same rotation frequency (20 Hz), Imp 1 shows two peaks in the PDF, with an increase of fluctuations from 40 to 160 mbar with radius. The pressure fluctuations are limited below 40 mbar for Imp 2 and 3, only one peak is found for Imp 2 at all the radius, while two peaks can be observed for Imp 3 at a rotation frequency ≥20 Hz. These results are consistent with the fluctuation intensity represented by standard deviation. Previously, the peak-to-peak value was extracted to inform the fluctuating intensity [30], but this method is inappropriate for Imp 2 and 3.

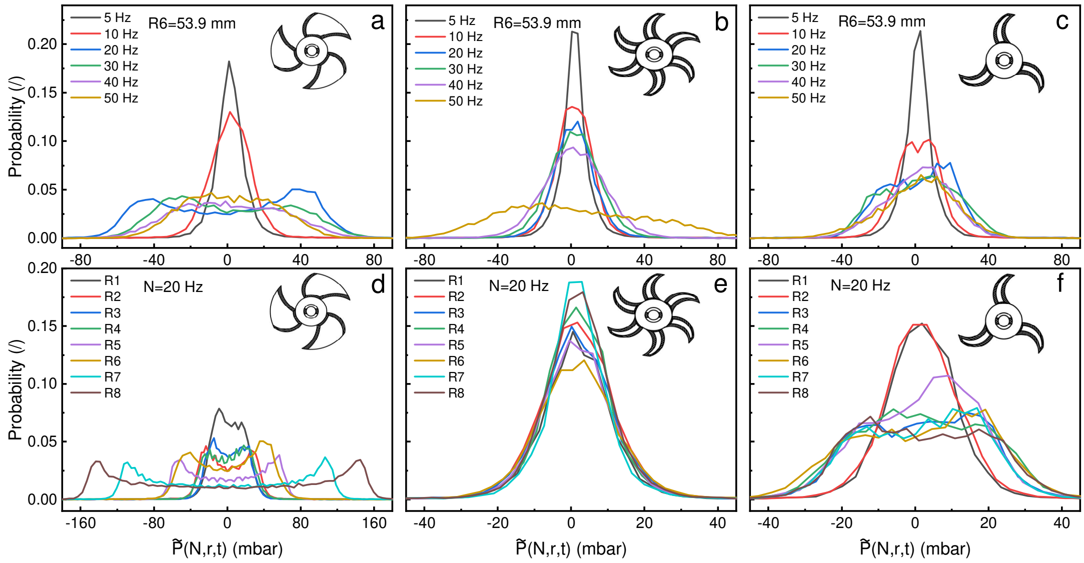

Fig. 9 PDF at different conditions. (a), (b) and (c) are the PDF versus rotation frequency for three impellers; (d), (e) and (f) are the PDF versus radius for three impellers.

3.3.3 FFT

With FFT, the time variations of pressure are presented on frequency domain. A rotation frequency of 20 Hz is selected as the representative displayed in Fig. 10. For three blades impellers (Imp 1 and 3), the significant peak amplitudes are found at N, $2N$, $3N$, $4.25N$ and $6N$, where N is the rotation frequency. The value of $3N$ demonstrates that the main frequency can be associated with the rotation frequency and the number of blades. N and $2N$ indicate the effects of one and two blades, while $6N$ is linked to twice the number of blades. The same peaks can be observed with six blades impeller, but $12N$ amplitude is almost negligible in the spectrum. In addition, another peak amplitude can be found at $4.25N$ for the three different impellers, with intensities around 1 mbar. It remains unclear for the pressure fluctuations during mixing. Compared to the amplitude at $3N$, there is an increase with the radius for Imp 1, even reaching up to 100 mbar at R8. Imp 3 also shows the same behaviour but with lower amplitude. Whereas the amplitude for Imp 2 is almost constant at all the radius.

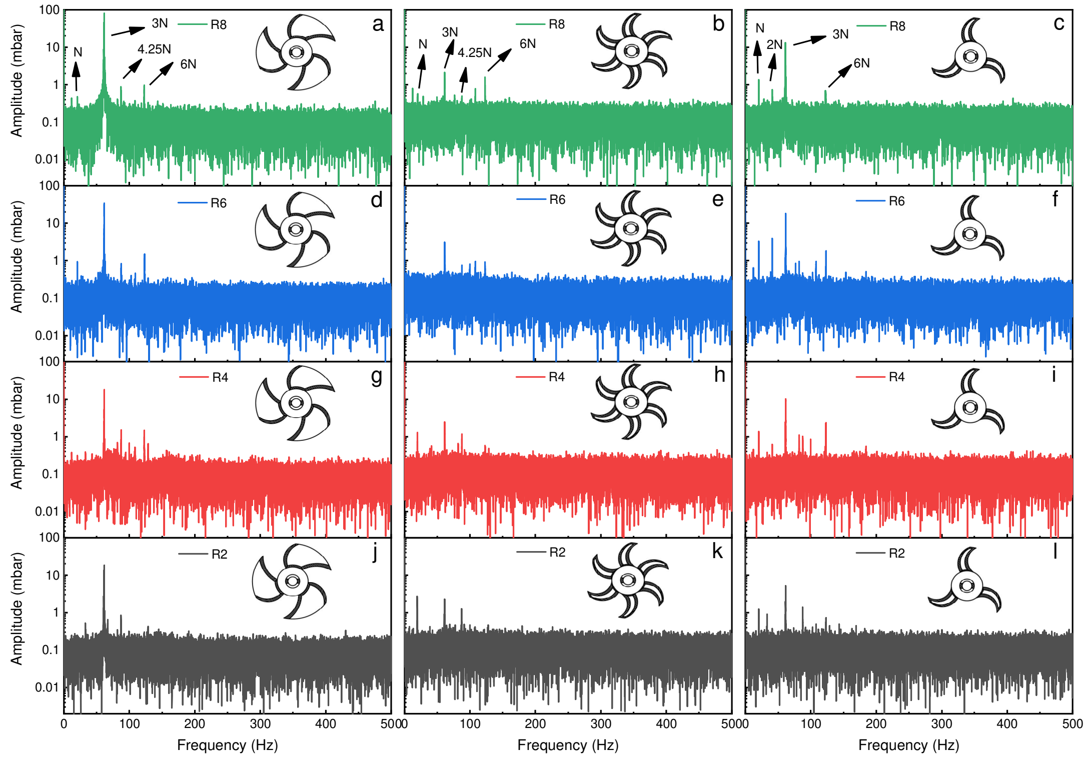

Fig. 10 Frequency domain analysis with FFT at 20 Hz. (a), (d), (g) and (j) are Imp 1; (b), (e), (h) and (k) are Imp 2; (c), (f), (i) and (l) are Imp 3.

Fig. 11 shows the cumulative amplitude of pressure fluctuations for *N*, *2N*, *3N*, *4.25N* and *6N* at R6 for the three impellers. This type of representation appears to be very useful to enhance the dominant frequencies, i.e., the frequencies associated with the higher amplitudes in FFT analysis plotted in Fig. 10. It can be seen in Fig. 11a that the cumulative amplitude increases significantly with the rotation frequency until 22.5 Hz, and then decreases for Imp 1. This behaviour is similar to one of the standard deviations plotted in Fig. 7a. The dominant frequencies are *6N* below 10 Hz and *3N* above 10 Hz. For Imp 2 (Fig. 11b), the cumulative amplitude is very weak, below 10 mbar. We find that the dominant frequencies are *6N* from 5 to 15 Hz, change to *3N* from 17.5 to 35 Hz, finally to be *N* from 40 to 50 Hz. It indicates that there is an increase of the contribution of the frequency *N* (one-blade effect) at higher rotation frequency. Furthermore, it should be noted that the cumulative amplitude does not increase at 50 Hz as it appears in σ_P, which means that this increase of pressure fluctuations is generated by a random component instead of a periodic signal. For Imp 3 (Fig. 11c), with the increase of rotation frequency, the dominant frequencies evolve from *6N* (5-10 Hz) to *3N* (12.5-30 Hz) and *2N* (35 Hz), finally by *N* (40-50 Hz). The cumulative amplitudes also differ somewhat from σ_P, especially for the value of *N* associated with the maximum fluctuations (cumulative amplitude at 30 Hz, σ_P at 25 Hz). It can be concluded that the random signal is not so important in the pressure fluctuations of Imp 1, while it has a greater effect in the case of Imp 2 and 3.

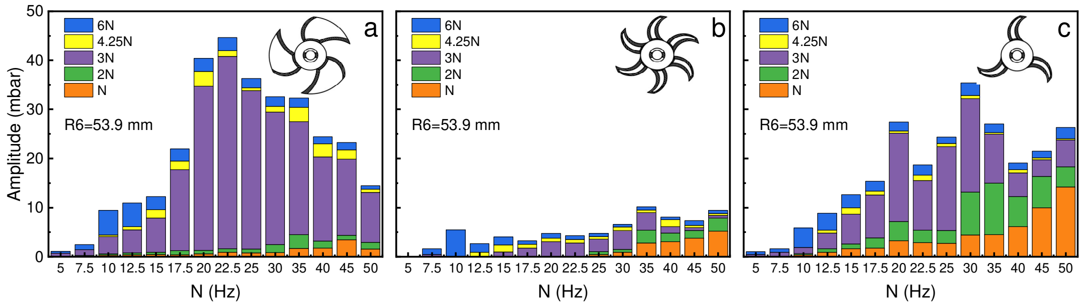

Fig. 11 Cumulative amplitudes at R6. (a) Imp 1; (b) Imp 2; (c) Imp 3.

3.3.4 Modelling

As explained in section 2.2.3, a model is proposed to reconstruct the PDF of pressure fluctuations from the convolution of a periodic and a random signal. The model parameters are determined from the minimisation of the cumulative error function: $\Delta \leq 0.3$. The plots of Fig. 12a, b and c show the phase diagram of total intensities versus rotation frequency and radius at the membrane surface. With the same legend, the total energy input for Imp 1 can reach up to 100 mbar at 20 Hz, which is much higher than the maximum value from Imp 2 and 3. The more intensive fluctuations occur at a high rotation frequency ($N>40$ Hz) for Imp 2, and from 20 to 40 Hz for Imp 3. These total energy inputs are consistent with σ_P, indicating a high degree of model validity. For random signal, the I_R is limited below 30 mbar for the three impellers. The relative periodic contribution $I_P/(I_P+I_R)$ are presented in Fig. 12d, e and f. It is found that the periodic fluctuations for Imp 1 dominate for most conditions (15-40 Hz), while they only appear at 20 to 30 Hz for Imp 3. Due to the weak amplitude observed in Fig. 11b for Imp 2, the periodic contribution remains below 50%. Thus, the use of Imp 1 is more appropriate than Imp 2 and 3 to intensify the pressure fluctuations at the membrane surface.

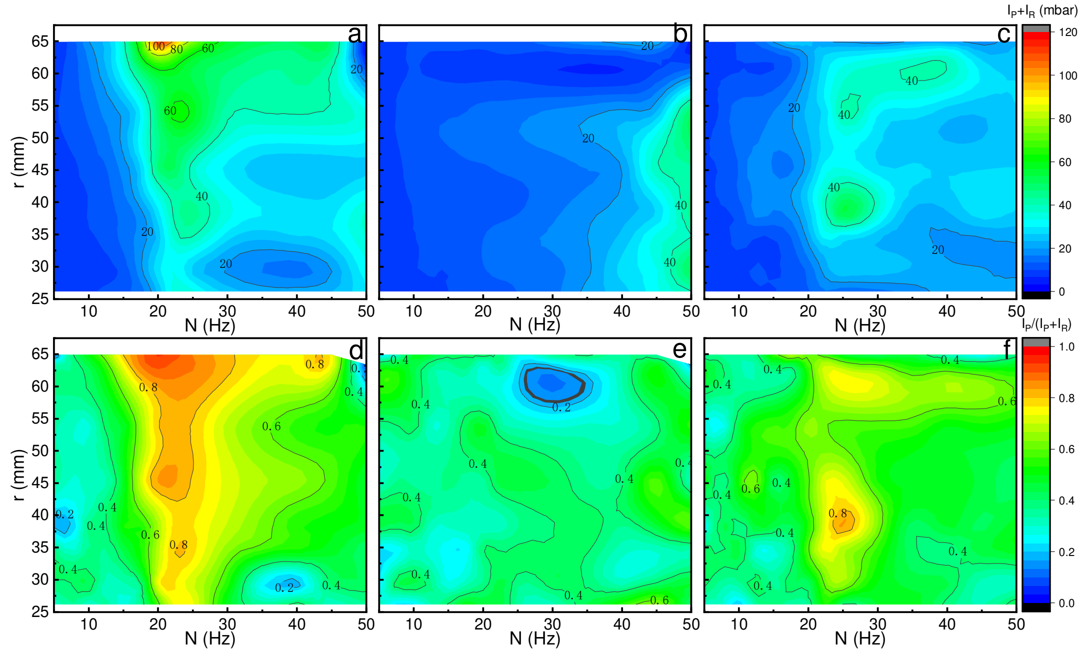

Fig. 12 Total energy input I_P+I_R (a, b, c) and periodic contribution I_P/(I_P+I_R) (d, e, f) as a function of rotation frequency and radius for Imp 1, Imp 2 and Imp 3, respectively.

The regression of intensity versus rotation frequency (*N*, Hz) and radius (*r*, m) can be a useful way to estimate the pressure fluctuations. It is plotted in Fig. 13. For periodic fluctuations (I_P, mbar), the fluid flow resonates under the periodic rotation of the impeller. On the membrane surface, the periodic pressure fluctuations evolve similarly to the response amplitude *U(ω)* of a second-order linear system to a periodic input force $F = F_0 \sin(\omega t)$ [35], which follows the equation:

$$U(\omega) = \frac{G F_0}{\sqrt{(1 - s^2)^2 + (2\epsilon s)^2}} \qquad (14)$$

where $s = \omega/\omega_0$ is the pulsation ratio. Here, we recognise the three parameters of the second order system: *G* is the gain, ω_0 is the intrinsic pulsation and ϵ the damping coefficient. However, the input signal $F' = F_0 \omega r \sin(\omega t)$ varies as a function of *ω* and *r* in our system, Eq.(14) was then modified to obtain a new function $U'(\omega)$. It can be written as:

$$U'(\omega) = \frac{G F_0 r^2 s^2}{\sqrt{(1 - s^2)^2 + (2\epsilon s)^2}} \qquad (15)$$

With slight modifications, a new model based on rotation frequency and local radius is proposed as in Eq.(16); the corresponding resonance frequency (N_r) of the system is calculated using Eq. (17).

$$I_P(N,r) = \frac{K}{\sqrt{(1-s^2)^2 + (2\epsilon s)^2}} \times \rho N^2 r^2$$
$$= \frac{K N_0^2}{\sqrt{(N_0^2 - N^2)^2 + (2\epsilon N_0 N)^2}} \times \rho N^2 r^2 \tag{16}$$

$$N_r = \frac{N_0}{\sqrt{1-2\epsilon^2}} \tag{17}$$

where $K = \frac{GF_0}{\rho N_0^2}$ and ϵ are constants, N_0 is the intrinsic frequency of the fluid in the cell. After regression, N_0 is equal to 20.6 Hz, which is slightly lower than the resonance frequency (21.1 Hz). Meanwhile, the values of K and ϵ are solved as 1.5 and 0.15, respectively.

For the random signal, I_R is found to be independent of the radius and to slightly increase with the rotation frequency. Then a linear regression is used to approximate the variations of random intensity as a function of N, which give a 90% prediction band with $I_R \pm 3.4$ mbar.

$$I_R = 0.21N + 4.8 \tag{16}$$

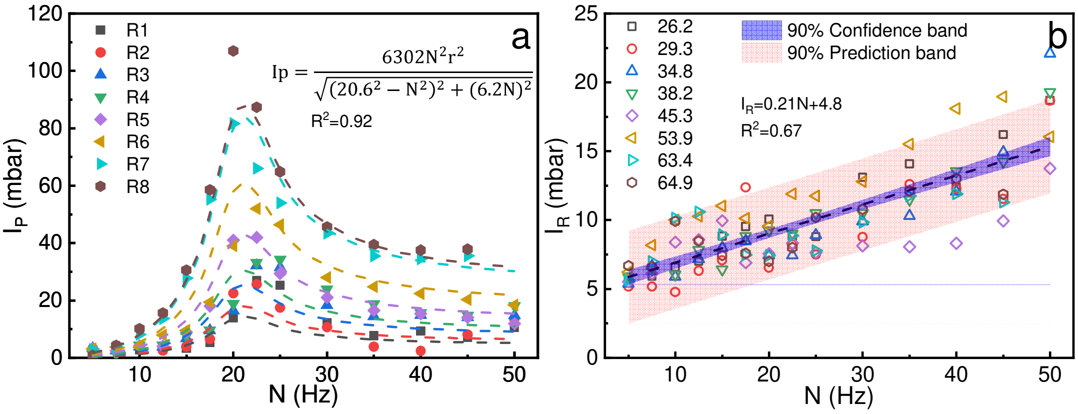

Fig. 13 Fluctuating intensities for Imp 1 as a function of rotation frequency and radius. (a) periodic intensity; (b) random intensity.

3.4 Signal reconstruction

Table. 1 Signal reconstruction for Imp 1 at R6, with the value of the two parameters to estimate the instantaneous pressure. A and σ are calculated from Eq. (14) and (15).

N (Hz)	P_0	ΔP_{mixing}	$\widetilde{P_P}(t)$		$\widetilde{P_R}(t)$
	Constant (mbar)	k (/)	A (mbar)	f (Hz)	σ (mbar)
10	294.5	0.59	5.5	3N	6.9
20			58	3N	9

30	32.3	3N	11.1
40	24.4	3N	13.2
50	21.8	3N	15.3

At different rotation frequencies, the local pressure of the steady flow without rotation (P_0) is almost constant with the same back pressure (300 mbar) and flowrate (50 L/h). ΔP_{mixing} is calculated with the mean k value equal to 0.59 obtained in section 3.2.2. The model parameters A and σ are determined from experimental data as explained in section 3.3.4. The dominant frequency is chosen equal to $3N$. φ does not affect the signal fluctuations and can be ignored. The time variations of pressure calculated from the model are compared with the experimental data and shown in Fig. 14. It can be noticed that the reconstructed signal provides a good description of the instantaneous pressure. Thus, this indicates that we can make use of this simplified model or estimate the time variations of the local pressure.

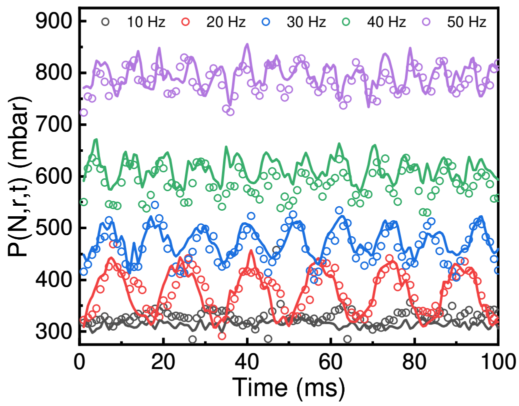

Fig. 14 Signal reconstruction of instantaneous pressure with empirical correlations (continuous and fluctuating components at R6) for Imp 1. Dots and lines correspond to the experimental and reconstructed signal, respectively.

4 Conclusions

DF has shown promise in reducing filter cake layer build-up, fouling accumulation and concentration polarisation. The enhanced filtration performance is attributed to the local shear as well as the pressure-driven force at the membrane surface in the RVF modules. The local shear rate has been widely discussed in the literature. In contrast, the present study exhibits new insight on the local pressure and in particular on the pressure fluctuations.

By the regression of ΔP_{mixing} curves, it is found that the core velocity coefficient, k values are higher at filtration cell entrance close to the shaft (lower radius, R1) due to the small cross-section and the low contribution of angular velocity. The mean values of k follow the order: Imp 2>Imp 1>Imp 3. It is concluded that the mixing pressure can be affected by the number of blades, then the impeller surface area.

The analysis of pressure fluctuations (SA, PDF, FFT) confirm that the magnitude following the same trends: Imp 1> Imp 3> Imp 2. At 20 Hz, σ_P (SA) of Imp 1 can reach up to 25% of TMP, while these values are negligible (<10%) for Imp 2 and 3. Considering FFT, the dominant frequency identified with Imp 1 is equal to 3 times the rotation frequency *(3N)*. On the contrary, different frequencies (*6N*, *3N* and *N*) exhibiting low amplitude are observed for Imp 2 and 3.

Based on the PDF modelling, periodic and random contributions are extracted by deconvolution of the time signal. Then, the empirical correlations are established to estimate their intensities as a function of rotation frequency and radial position. The intensity of the random pressure fluctuations is limited to 30 mbar for all impellers. The periodic contribution is dominant for Imp 1, and a "resonance frequency" of 21.1 Hz is clearly identified. Considering fluctuating pressure analysis and modelling, Imp 1 appears as the best candidate for microfiltration applications. However, other criteria such as local shear rate and filtration performances (instantaneous and local permeate flux or hydraulic resistance) could also be used to select optimal impeller and operating conditions.

This work provides a better fundamental knowledge for the characterization and the modelling of instantaneous pressure at the membrane surface in a dynamic filtration module; it highlights the potential of pressure fluctuations as an additional driving force to intensify microfiltration and also to better optimise the impeller configuration. Nevertheless, for better performance in DF (enhanced permeate flux and reduced fouling), the optimal impeller configuration requires further simulation and verification based on shear fluctuation include pressure as well as shear stress. A theoretical explanation for the time variations of pressure (resonance phenomenon) also deserves further development.

Nomenclature

A	Amplitude, mbar
A_f	Amplitude at frequency f, mbar
F	Flatness, /
f	Frequency, Hz
G	Gain of the system, /
I_P	Periodic intensity, mbar
I_R	Random intensity, mbar
K	Numerical coefficient, /
k	Core velocity coefficient, /
m	Sampling number, /
N	Rotation frequency of the impeller, Hz
N_0	Intrinsic frequency, Hz
N_r	Resonance frequency, Hz
$P(f)$	Pressure at frequency f, mbar
P_0	Pressure without the rotation of impeller, mbar
$P(r,t)$	Instantaneous pressure, mbar
$\widetilde{P_P}(t)$	Periodic signal, mbar
$\widetilde{P_R}(t)$	Random signal, mbar
$\bar{P}(N,r)$	Mean time pressure, mbar
$\tilde{P}(N,r,t)$	Fluctuating pressure, mbar
Q_F	Feeding flowrate, m^3/s
r	Radius at membrane surface, m
R_0	Inner radius of the membrane, m
R_m	Outer radius of the membrane, m
S	Skewness, /
T_{inlet}	Inlet temperature, °C
T_{outlet}	Outlet temperature, °C
$\bar{u}$	Mean velocity of fluid, m/s
β	Coefficient of variation, /
ϵ	Dumping factor, /
ρ	Fluid density, kg/m^3
σ	Standard deviation of random signal, mbar
σ_P	Standard deviation of fluctuating pressure, mbar
φ	Phase, °
Δ	Minimum cumulative error, /
ΔP_{mixing}	Additional pressure generated by the rotating impeller, mbar

Acknowledgments

Financial support from the China Scholarship Council is gratefully acknowledged (grant No. 201801810069). Thanks to Pascal DEBREYNE and Jacky SIX (INRAE,

Lille) for the realisation of the experimental device about the instantaneous and local pressure measurement.

References

[1] M. Cheng, X. Xie, P. Schmitz, L. Fillaudeau, Extensive review about industrial and laboratory dynamic filtration modules: Scientific production, configurations and performances, Separation and Purification Technology, 265 (2021) 118293.

[2] M.Y. Jaffrin, Dynamic shear-enhanced membrane filtration: A review of rotating disks, rotating membranes and vibrating systems, Journal of Membrane Science, 324 (2008) 7-25.

[3] L. Ding, M.Y. Jaffrin, J. Luo, Chapter Two - Dynamic Filtration with Rotating Disks, and Rotating or Vibrating Membranes, in: S. Tarleton (Ed.) Progress in Filtration and Separation, Academic Press, Oxford, 2015, pp. 27-59.

[4] P. Mikulasek, Methods to reduce concentration polarization and fouling in membrane filtration, Collect. Czech. Chem. Commun., 59 (1994) 737-755.

[5] O.A. Akoum, M.Y. Jaffrin, L. Ding, P. Paullier, C. Vanhoutte, An hydrodynamic investigation of microfiltration and ultrafiltration in a vibrating membrane module, Journal of Membrane Science, 197 (2002) 37-52.

[6] L.-H. Ding, O. Akoum, A. Abraham, M.Y. Jaffrin, High shear skim milk ultrafiltration using rotating disk filtration systems, AIChE Journal, 49 (2003) 2433-2441.

[7] M. Frappart, M. Jaffrin, L.H. Ding, Reverse osmosis of diluted skim milk: Comparison of results obtained from vibratory and rotating disk modules, Separation and Purification Technology, 60 (2008) 321-329.

[8] L. Chen, Y. Qiu, Removal of Cd (II) from dilute aqueous solutions by complexation–ultrafiltration using rotating disk membrane and the shear stability of PAA–Cd complex, Chinese Journal of Chemical Engineering, 27 (2019) 519-527.

[9] R. Bouzerar, M. Jaffrin, L.-H. Ding, P. Paullier, Influence of Geometry and Angular Velocity on Performance of a Rotating Disk Filter, AIChE Journal, 46 (2000) 257-265.

[10] K.-J. Hwang, S.-E. Wu, Disk structure on the performance of a rotating-disk dynamic filter: A case study on microalgae microfiltration, Chemical Engineering Research and Design, 94 (2015) 44-51.

[11] K.-J. Hwang, S.-E. Wu, Y.-L. Hsueh, Analysis on the nonuniformity of cake formation in rotating-disk dynamic microfiltration, Separation and Purification Technology, 198 (2018) 16-24.

[12] H.S. Marke, M.P. Breil, E.B. Hansen, M. Pinelo, U. Krühne, Investigation of the velocity factor in a rotational dynamic microfiltration system, Separation and Purification Technology, 220 (2019) 69-77.

[13] L. Ding, M. Jaffrin, M. Mellal, G. He, Investigation of performances of a multishaft disk (MSD) system with overlapping ceramic membranes in microfiltration of mineral suspensions, Journal of Membrane Science, 276 (2006) 232-240.

[14] T.K. Sherwood, P.L.T. Brian, R.E. Fisher, Desalination by Reverse Osmosis, Industrial & Engineering Chemistry Fundamentals, 6 (1967) 2-12.

[15] M. Hapońska, E. Clavero, J. Salvadó, C. Torras, Application of ABS membranes in dynamic filtration for Chlorella sorokiniana dewatering, Biomass and Bioenergy, 111 (2018) 224-231.

[16] M. Mertens, M.R. Bilad, A.Y. Gebreyohannes, L. Marbelia, I.F.J. Vankelecom, Membrane development for improved performance of a magnetically induced vibration system for anaerobic sludge filtration, Separation and Purification Technology, 200 (2018) 120-129.

[17] G. Genkin, T. Waite, A. Fane, S. Chang, The effect of vibration and coagulant addition on the filtration performance of submerged hollow fibre membranes, Journal of Membrane Science, 281 (2006) 726-734.

[18] J.C. Kim, F. Garzotto, D.N. Cruz, A. Clementi, F. Nalesso, J.H. Kim, E. Kang, H.C. Kim, C. Ronco, Computational modeling of effects of mechanical shaking on hemodynamics in hollow fibers, Int. J. Artif. Organs, 35 (2012) 301-307.

[19] R. Holdich, K. Schou, M. Dragosavac, S. Kellet, H. Bandulasena, A comparison of azimuthal and axial oscillation microfiltration using surface and matrix types of microfilters with a cake-slurry shear plane exhibiting non-Newtonian behaviour, Journal of Membrane Science, 550 (2018) 357-364.

[20] B. Wu, Y. Zhang, Z. Mao, W.S. Tan, Y.Z. Tan, J.W. Chew, T.H. Chong, A.G. Fane, Spacer vibration for fouling control of submerged flat sheet membranes, Separation and Purification Technology, 210 (2019) 719-728.

[21] L. Fillaudeau, B. Boissier, S. Ermolaev, N. Jitariouk, Etude hydrodynamique d'un module de filtration dynamique, Ind. Alim. Agri., 124 (2007) 8-16.

[22] X. Xie, C. Le Men, N. Dietrich, P. Schmitz, L. Fillaudeau, Local hydrodynamic investigation by PIV and CFD within a Dynamic filtration unit under laminar flow, Separation and Purification Technology, 198 (2018) 38-51.

[23] T.R. Bentzen, N. Ratkovich, S. Madsen, J.C. Jensen, S.N. Bak, M.R. Rasmussen, Analytical and numerical modelling of Newtonian and non-Newtonian liquid in a rotational cross-flow MBR, Water Sci Technol, 66 (2012) 2318-2327.

[24] A. Chaudhuri, A. Jogdand, Permeate flux decrease due to concentration polarization in a closed roto-dynamic reverse osmosis filtration system, Desalination, 402 (2017) 152-161.

[25] M.Y. Jaffrin, L.-H. Ding, O. Akoum, A. Brou, A hydrodynamic comparison between rotating disk and vibratory dynamic filtration systems, Journal of Membrane Science, 242 (2004) 155-167.

[26] T. Zsirai, H. Qiblawey, M.J. A-Marri, S. Judd, The impact of mechanical shear on membrane flux and energy demand, Journal of Membrane Science, 516 (2016) 56-63.

[27] S.P. Beier, G. Jonsson, Critical flux determination by flux-stepping, AIChE Journal, 56 (2009) 1739-1747.

[28] J. Luo, L. Ding, Y. Wan, M.Y. Jaffrin, Threshold flux for shear-enhanced

nanofiltration: Experimental observation in dairy wastewater treatment, Journal of Membrane Science, 409-410 (2012) 276-284.

[29] A. Brou, L. Ding, P. Boulnois, M.Y. Jaffrin, Dynamic microfiltration of yeast suspensions using rotating disks equipped with vanes, Journal of Membrane Science, 197 (2002) 269-282.

[30] M. Cheng, C. Le Men, A. Line, P. Schmitz, L. Fillaudeau, Methodology to investigate instantaneous and local transmembrane pressure within Rotating and Vibrating Filtration (RVF) module, Separation and Purification Technology, (2021) 118955.

[31] L. Fillaudeau, B. Boissier, A. Moreau, P. Blanpain-Avet, S. Ermolaev, N. Jitariouk, Investigation of rotating and vibrating filtration for clarification of rough beer, Journal of Food Engineering, 80 (2007) 206-217.

[32] L. Broussous, P. Schmitz, H. Boisson, E. Prouzet, A. Larbot, Hydrodynamic aspects of filtration antifouling by helically corrugated membranes, Chemical Engineering Science, 55 (2000) 5049-5057.

[33] Y.E. Rayess, Y. Manon, N. Jitariouk, C. Albasi, M.M. Peuchot, A. Devatine, L. Fillaudeau, Wine clarification with Rotating and Vibrating Filtration (RVF): Investigation of the impact of membrane material, wine composition and operating conditions, Journal of Membrane Science, 513 (2016) 47-57.

[34] X. Xie, Investigation of Local and Global Hydrodynamics of a Dynamic Filtration Module (RVF Technology) for Intensification of Industrial Bioprocess, in: LISBP, INSA Toulouse, 2017.

[35] S.G. Kelly, Mechanical vibrations: theory and applications, Cengage learning, 2012.